Cite this: DOI: 10.1039/xxxxxxxxxx

Wall entrapment of peritrichous bacteria: A mesoscale hydrodynamics simulation study†

S. Mahdiyeh Mousavi, Gerhard Gompper, and Roland G. Winkler

Received Date
Accepted Date

DOI: 10.1039/xxxxxxxxxx

www.rsc.org/journalname

Microswimmers such as *E. Coli* bacteria accumulate and exhibit an intriguing dynamics near walls, governed by hydrodynamic and steric interactions. Insight into the underlying mechanisms and predominant interactions demand a detailed characterization of the entrapment process. We employ a mesoscale hydrodynamics simulation approach to study entrapment of a *E. coli*-type cell at a no-slip wall. The cell is modeled by a spherocylindrical body with several explicit helical flagella. Three stages of the entrapment process can be distinguished: the approaching regime, where a cell swims toward the wall on a nearly straight trajectory; a scattering regime, where the cell touches the wall, with an reorientation of the cell by a torque originating from steric interactions; and a surface-swimming regime. Our simulations show that steric interactions may dominate the entrapment process, yet, hydrodynamic interactions slow down the adsorption dynamics close to the boundary and imply a circular motion on the wall. The locomotion of the cell is characterized by a strong wobbling dynamics, with cells preferentially pointing toward the wall.

1 Introduction

Surfaces and walls play an essential role in the life cycle of bacteria, because in the wild, bacteria are only rarely isolated and free-swimming, but are primarily associated with surfaces.[1–3] In fact, bacteria typically spend most of their life time in a biofilm, rather than as planktonic cell in the bulk fluid, yet biofilm formation is initiated by an initial contact of a planktonic cell with a surface.[4,5] Bacteria approaching a wall experience surface-specific interactions, such as hydrodynamic forces, adhesive forces, steric interactions, etc., which govern the adsorption process and their surface dynamics. The importance of the various interactions for bacteria entrapment has been addressed experimentally, theoretically, and by simulations. Studies on wall entrapment of microorganisms, such as non-tumbling *E. coli*[6] and bull spermatozoa[7], reveal an enhanced concentration at a surface. This near-wall accumulation of cells can be explained by two distinct mechanisms.[8–10] On the one hand, hydrodynamic interactions between the microswimmer and the wall lead to an attractive interaction and, for *E.coli*-type bacteria, a torque trying to align the microswimmer with the surface.[6,11] On the other hand, neglecting explicit hydrodynamic interactions, the cell body of a flagellated microswimmer, e.g., *E. coli*, moving along a no-slip wall at constant height experiences viscous drag and a torque rotates the body.[11–13] At the same time, the flagellar bundle is exposed to this torque, which rotates it away from the wall, and a second torque originated from the coupling to the cell translational motion. Since the overall system is torque free, a finite inclination angle of the flagellum is obtained with the cell swimming toward the wall.[2,11,14] Finally, in addition to the hydrodynamic mechanisms for the near wall accumulation, steric interactions with a wall and cell rotational Brownian motion alone can also produce wall accumulation at finite microswimmer density.[15–17]

Despite considerable efforts, the process of microswimmer entrapment at walls is by no means satisfactorily described by explicit modeling so far. Various numerical studies, using the boundary-element method and representing a bacterium by a rigid spheroidal body and the flagella bundle by an attached aligned thin helical cylinder, predict stable configurations of cells swimming at a planar wall.[18,19] Cells are found to maintain a stable height above a surface with an inclination angle, where the bacterium's body points away from the wall. Moreover, recent studies on bacteria-like polar swimmer, consisting of a spheroidal body and an active propelling rod, predict a critical swimmer size for entrapment.[8] Regardless of the cell body shape, organisms with sufficiently long flagella—about twice the cell-body diameter—are expected to exhibit a positive inclination angle with the head pointing toward the boundary, whereas for short enough flagella, they are orientated away from the wall. This effect can be traced back to a faster increase of the Stokeslet dipole and quadrupole strengths with increasing rod length compared to the source dipole strength.[8] Mesoscale hydrodynamics simulations of a mechano-elastic *E. coli*-type model with several explicit

Theoretical Soft Matter and Biophysics, Institute of Complex Systems and Institute for Advanced Simulation, Forschungszentrum Jülich and JARA, D-52425 Jülich, Germany

flagella, including thermal noise and steric interactions, also yield stable, wall-parallel trajectories with a distance of approximately $250nm$, about half of a body radius, between the wall and the cell-body surface.[20] Similar simulations of a more complex, swarmer-type bacteria model,[21] with an elongated body and a large number of randomly anchored flagella, exhibit stable entrapped trajectories with cells preferentially oriented toward the wall. The elongated nature of the cell body leads to a large (average) angle between the cell body and the inclined bundle. The interplay of near-field hydrodynamic wall interactions and steric repulsion of cell body and bundle determines then the orientation toward the wall. A recently developed experimental setup enables the full three-dimensional characterization of the entrapment dynamics of smoothly swimming *E. coli* bacteria.[22,23] Such studies clearly reveal a significant angle between the cell body and the surface, with a rather broad angle distribution, but cells pointing toward the wall. Hence, there is a disparity of available results and lack of a clear understanding of the entrapment mechanism at walls. The insight into the corresponding cell-level processes is not only fundamental for biological systems, e.g., biofilm initiation, but should also be essential for the rational design of biomimetic microrobots.[24,25]

In this article, we perform mesoscale-hydrodynamics simulations of a mechano-elastic *E. coli*-type model with several flagella to shed light onto the entrapment of bacteria at a no-slip surface. Our bacterium model closely resembles the geometry, flagellar elastic properties, and rotary motor torque of *E. coli* with multiple flagella.[21,26] A hybrid simulation approach is adopted, where molecular dynamics simulations for the bacterium are combined with the multiparticle collision dynamics (MPC) method for the embedding fluid.[27] MPC is a particle-based simulation approach taking into account hydrodynamic interactions and thermal fluctuations.[28–30] It is a valuable and adequate simulation method to study nonequilibrium, active systems.[10,17,20,21,26,29,31–39] In particular, MPC has successfully been used to characterize synchronization of flagella beating between nearby swimming sperm,[40] bundling of helical flagella of bacteria,[41,42] swimming of bacteria near walls,[20,21], and studies on clustering of squirmers.[43]

In our simulations, the cell entrapment process can be classified in three regimes, the approaching regime, where cells swim essentially straight toward the surface, the scattering regime, where they reorient, and the surface swimming regime, where they swim along the wall on circular trajectories. We confirm that hydrodynamic interactions reduce the swimming velocity while they approach the surface, however, it is rather due to lubrication than hydrodynamic interactions by the force-dipole flow field. Similarly, reorientation is caused by steric cell-surface interactions and/or hydrodynamics.[23,44] In contrast to the various theoretical predictions, our cells preferentially point toward the surface during stable near wall locomotion. Since we consider randomly anchored flagella on the cell surface, we find a wide spectrum of wobbling motions, where the cell body's orientation varies periodically.[45] Interestingly, the bundle orientation and overall swim direction is little affected by the strong orientational fluctuations of the cell body. Evidently, the flagella bundle rotation determines the overall cell swimming behavior and the cell body responds to the this rotation.

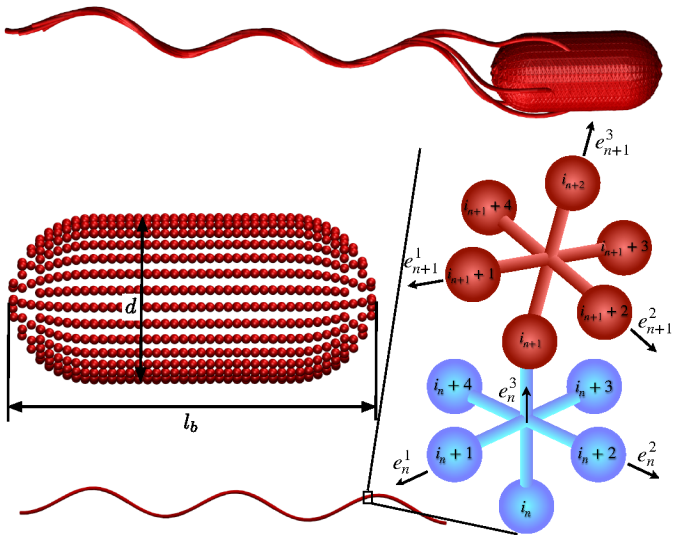

Fig. 1 Model of an *E. coli* cell with a spherocylindrical cell body of diameter $d = 0.9\mu m$ and length $l_b = 2.5\mu m$. It is composed of circular sections of particles, which are connected by the bond potential of Eq. (1). The flagellum, a three-turn left-handed helix of radius $R = 0.2\mu m$, pitch $L = 2.2\mu m$ and contour length $L_c = 7.6\mu m$ consists of 76 consecutive octahedral-like segments.

The manuscript is organized as follows. In Sec. 2, the cell model and simulation approach are described. Section 3 presents the results for the various stages of the scattering process, and Sec. 4 summarizes our findings.

2 Simulation method

2.1 *E. coli* model

We employ a mechano-elastic bacterium model.[20,21,26]. The cell is composed of a spherocylindrical body and flagella modelled by semiflexible helical filaments (cf. Fig. 1). The whole cell is constructed by points of mass M. For the body, the points are arranged on the circumference and in the center of circles of diameter $d = 9a$, a is the length unit related to the MPC fluid described in Sec. 2.2, with a spacing of $0.5a$ (along the cylinder center line) and on smaller circles toward the poles. The cylindrical part consists of 22 and the spherical cap of nine such circles corresponding to the body length $l_b = 20a$. In order to preserve the stability of the body, nearest and next-nearest-neighboring particles are connected by a harmonic potential of the form

$$U_b = \frac{1}{2}K_b(r - r_e)^2, \tag{1}$$

where r and r_e are the distance between a particle pair and its preferred value, respectively, and K_b is the bond strength. Each bacterium is equipped with 5 randomly anchored flagella, which are described by the helical wormlike chain model,[46,47] with an adaptation suitable for the combination with MPC.[26] A flagellum consists of $N = 76$ segments of 6 particles arranged in an octahedral shape, with 12 bonds along the edges of length $a/\sqrt{2}$ and 3 along the diagonals of length a. This construction allows for the intrinsic twist of the flagellum and its coupling to MPC particles

capturing torsional fluctuations.

Introducing the orthogonal bond vectors $\boldsymbol{b}_n^1 = \boldsymbol{r}_{i_n+1} - \boldsymbol{r}_{i_n+3}$, $\boldsymbol{b}_n^2 = \boldsymbol{r}_{i_n+2} - \boldsymbol{r}_{i_n+4}$, and $\boldsymbol{b}_n^3 = \boldsymbol{r}_{i_n+1} - \boldsymbol{r}_{i_n}$ for the bonds along the contour of the flagellum, we can define orthonormal triads $\{\boldsymbol{e}_n^1, \boldsymbol{e}_n^2, \boldsymbol{e}_n^3\}$, $n = 1, \ldots, N$, where $\boldsymbol{e}_n^\alpha = \boldsymbol{b}_n^\alpha / |\boldsymbol{b}_n^\alpha|$, $\alpha \in \{1,2,3\}$ (cf. Fig. 1). The local elastic deformation of a flagellum proceeds in two steps: (i) the rotation of $\{\boldsymbol{e}_n^1, \boldsymbol{e}_n^2, \boldsymbol{e}_n^3\}$ around $\boldsymbol{e}_n^3$ by a twist angle φ_n and (ii) the rotation of the twisted triad $\{\tilde{\boldsymbol{e}}_n^1, \tilde{\boldsymbol{e}}_n^2, \tilde{\boldsymbol{e}}_n^3\}$ by a bending angle ϑ_n around the normal $\boldsymbol{n}_n = (\boldsymbol{e}_n^3 \times \boldsymbol{e}_{n+1}^3)/|\boldsymbol{e}_n^3 \times \boldsymbol{e}_{n+1}^3|$ to the plane defined by the contour bonds $\boldsymbol{b}_n^3$ and $\boldsymbol{b}_{n+1}^3$. The elastic deformation energy is then

$$U_{el} = \frac{1}{2} \sum_{\alpha=1}^{3} K_{el}^\alpha \sum_{n=1}^{N-1} (\Omega_n^\alpha - \Omega_e^\alpha)^2, \tag{2}$$

where $K_{el}^1 = K_{el}^2$ is the bending modulus, K_{el}^3 the twist modulus, and $\boldsymbol{\Omega}_n = \Omega_n^1 \boldsymbol{e}_n^1 + \Omega_n^2 \boldsymbol{e}_n^2 + \Omega_n^3 \boldsymbol{e}_n^3 \equiv \vartheta_n \boldsymbol{n}_n + \varphi_n \boldsymbol{e}_n^3$ the strain vector. The parameters Ω_e^α define the equilibrium geometry of the model flagellum and are chosen to recover the shape of an *E. coli* flagellum in the normal state.[48]

A flagellum is attached to the body by randomly choosing a body particle as its first contour particle. The rotation of the flagellum is induced by a motor torque $\boldsymbol{T}$ decomposed into a force couple $\boldsymbol{F}$ and $-\boldsymbol{F}$ acting on particles i_1+2 and i_1+4 ($\boldsymbol{T} = \boldsymbol{b}_1^2 \times \boldsymbol{F}$ with $\boldsymbol{F}$ parallel to $\boldsymbol{b}_1^1$), or equivalently i_1+1 and i_1+3 ($\boldsymbol{T} = \boldsymbol{b}_1^1 \times \boldsymbol{F}$ with $\boldsymbol{F}$ parallel to $\boldsymbol{b}_1^2$). Moreover, an opposite torque $-\boldsymbol{T}$ is exerted on two body particles non-aligned with the body axis and on different circles in the vicinity of the anchoring point. Hence, the bacterium is force and torque free. A repulsive harmonic potential

$$U_{ex} = \begin{cases} \frac{1}{2} K_{ex} (r - r_{ex})^2 & r < r_{ex} \\ 0 & \text{otherwise} \end{cases} \tag{3}$$

is used to prevent flagella crossing and their penetration into the cell body. Here, r is the closest distance between contour bond segments of different flagella and the distance to the body-center particles. We set $r_{ex} = 0.25a$ and $r_{ex} = (d+a)/2$ for the flagellum-flagellum and flagellum-body interactions, respectively.

The forces resulting from the potentials (1)–(3) and the forces induced by the torques $\boldsymbol{T}$ and $-\boldsymbol{T}$ determine the dynamics of the bacterium, which is described by Newton's equation of motion. The latter are solved by the velocity Verlet integration scheme.[49]

2.2 Fluid model: multiparticle collision dynamics

The fluid is modeled as a collection of point particles of mass m with position $\boldsymbol{r}_i$ and velocity $\boldsymbol{v}_i$. The dynamics of the particles proceeds by alternating streaming and collision steps.[28–30] During a streaming step, particles move ballistically over a time interval Δt, denoted as collision time, and the their positions are updated according to

$$\boldsymbol{r}_i(t + \Delta t) = \boldsymbol{r}_i(t) + \boldsymbol{v}_i(t) \Delta t. \tag{4}$$

In the collision step, all particles are sorted in cubic collision cells of length a. Subsequently, the relative velocity of each particle, with respect to the center-of-mass velocity of the considered collision cell, is rotated by a fixed angle α around a randomly oriented axis, hence, their velocities after the collision are[50]

$$\boldsymbol{v}_i(t + \Delta t) = \boldsymbol{v}_{cm}(t) + \mathbf{R}(\alpha) \left[\boldsymbol{v}_i(t) - \boldsymbol{v}_{cm}(t) \right] - \boldsymbol{r}_{ic} \times \left[m \mathbf{I}^{-1} \sum_{j \in cell} \left(\boldsymbol{r}_{jc}(t) \times [\boldsymbol{v}_{jc}(t) - \mathbf{R}(\alpha) \boldsymbol{v}_{jc}(t)] \right) \right], \tag{5}$$

where $\mathbf{R}(\alpha)$ is the rotation operator, $\boldsymbol{v}_{cm}$ the center-of-mass velocity, $\boldsymbol{r}_{jc} = \boldsymbol{r}_j - \boldsymbol{r}_{cm}$, $\boldsymbol{v}_{jc} = \boldsymbol{v}_j - \boldsymbol{v}_{cm}$, and $\mathbf{I}$ the moment-of-inertia tensor of the particles in the center-of-mass reference frame of the collision cell of particle i. The collision rule (5) conserves both linear and angular momentum in each cell.[50–52] Discretization in collision cells implies violation of Galilean invariance, which is reestablished by a random shift of the collision-cell grid after every streaming step.[53] A constant temperature is maintained by a collision-cell-based, local Maxwellian thermostat, where the relative velocities of the particles in a collision cell are scaled according to the Maxwell-Boltzmann scaling (MBS) method.[54]

2.3 Coupling of bacterium and MPC fluid

The coupling between the MPC fluid and the bacterium is achieved in the MPC collision step by treating the points of the bacterium on equal footing with the MPC particles, i.e., their velocities are also rotated according Eq. (5) to ensure momentum exchange between them and the fluid.[21,27,55] Here, the center-of-mass velocity of a collision cell is given by

$$\boldsymbol{v}_{cm} = \frac{1}{m N_c + M N_c^c} \left(\sum_{i=1}^{N_c} m \boldsymbol{v}_i + \sum_{j=1}^{N_c^c} M \boldsymbol{v}_j^b \right), \tag{6}$$

where, N_c^c is the number of mass points of a bacterium in the considered collision cell. Note that the cell body is penetrable for fluid particles by this coupling. However, this still provides a no-slip boundary condition on the body surface.[56]

2.4 Wall interaction

The fluid is confined between two walls parallel to the xz plane of the Cartesian reference frame. No-slip boundary conditions are implemented by employing the bounce-back rule for MPC particles and by taking into account wall phantom particles.[30,54,57] To avoid direct wall contact, a cell experiences the repulsive Lennard-Jones potential (wall at $y = 0$)

$$U_W = \begin{cases} 4 k_B T \left[\left(\frac{\sigma}{y - y'} \right)^{12} - \left(\frac{\sigma}{y - y'} \right)^{6} + \frac{1}{4} \right] & y - y' < y_c \\ 0 & \text{otherwise} \end{cases}, \tag{7}$$

where y is either the distance between a flagellum contour particle and the wall, or that of a body center-line particles and the wall. Hence, $y' = d/2$ for cell body and $y' = 0$ for a flagellum particle.

2.5 Parameters

We choose $K_{el}^1 = K_{el}^2 = K_{el}^3 = 5 \times 10^4 k_B T$ within the range of experimentally measured values of the flagellar filaments.[26,47,48]

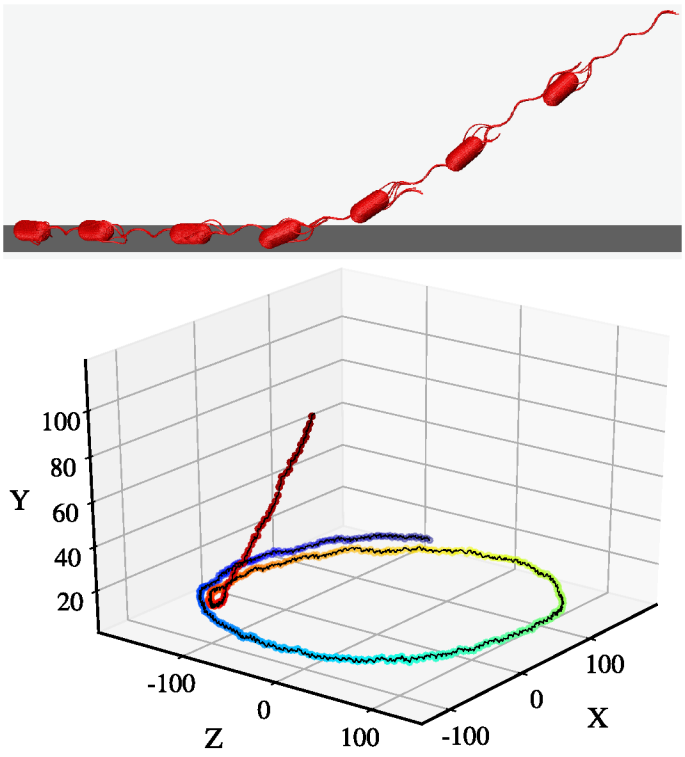

Fig. 2 Trajectory of a cell approaching a wall and undergoing a clockwise circular motion on the surface. The starting angle is $\theta_s = 45°$. (See supplementary files, movie M1)

Here, k_B is the Boltzmann factor and T the temperature. The magnitude of the torque is set to $|\boldsymbol{T}| = 400 k_B T = 1640\ pN nm$, smaller than the torque measured experimentally ($4500\ pN nm$) for a stalled motor.[20,58,59] As a consequence, the bundle rotates with the average frequency $\omega_{bund} = 3.14 \times 10^{-2}\sqrt{k_B T/ma^2}$, five times faster than the body, comparable to *E. coli* cells.[48] The force constant of the bonds and the repulsive harmonic potential are set to $K_b = K_{ex} = 10^4 k_B T/a^2$. The cut-off distance for the wall interaction is $y_c = \sqrt[6]{2}a$ and the interaction range is $\sigma = a$.

Length and time are measured in units of the collision cell size a and $\tau = a\sqrt{m/k_B T}$, respectively. We choose the collision time $\Delta t = 0.05\tau$ and the average number of fluid particles in a cell $\langle N_c \rangle = 10$. A cubic simulation box of length $200a$ is considered, with two no-slip walls parallel to the xz plane of the Cartesian reference frame and periodic boundary conditions parallel to the walls. At least ten independent realizations are considered for every shown parameter set.

3 Results

Initially, swimming cells are created by independent bulk simulations, with randomly anchored, radially outward pointing flagella. By applying independent torques $\boldsymbol{T}$ to rotate flagella, a bundle is formed and a cell starts to swim uni-directionally. Subsequently, the cell is placed in the center between the two walls and rotated such that its swimming direction forms an angle θ_s with the wall. The cell orientation of the subsequent trajectory is characterized by the inclination angle $\theta_i(t)$ between the main axis of the inertia tensor of the cell (body and flagella)—in fact, it closely agrees with the orientation of the flagellar bundle as well as the swimming direction—and its projection onto the horizontal wall (cf. Fig. 2) ($\theta_s = \theta_i(0)$).

As is well established, motile bacteria display helical swimming paths,[60] since the flagellar bundle is typically not aligned with the cell body, but can be strongly inclined.[21,61,62] The inclination causes a wobbling motion of the cell body, i.e., it precesses around the swimming direction.[22,23,61,63,64] Wobbling (wiggling) depends on different cell parameters such as the orientation and position of the flagellar bundle relative to the cell body, or the viscoelastic properties of the surrounding fluid.[63,64] We expect an effect of wobbling on the cell-surface scattering process.

Figure 2 depicts a cell approaching a wall and its clockwise swimming at the wall. The time dependence of the center-of-mass height above the wall is displayed in Fig. 3. Initially, a cell swims more or less straight toward the wall until it interacts with the wall. Subsequently, the cell moves along the wall at a nearly constant height in a circular manner.

Three regimes can be identified in Fig. 3(a): (i) The approaching regime $t/\hat{\tau} \lesssim 5$, where the inclination angle is fluctuating, but the cell swims essentially straight, (ii) the reorientation regime $5 \lesssim t/\hat{\tau} \lesssim 9$, and (iii) the surface swimming regime $t/\hat{\tau} \gtrsim 9$. Here, $\hat{\tau} = l_b/\bar{v} = 0.67 \times 10^4 \tau$ is the time required for a cell with the average velocity $\bar{v} = 3 \times 10^{-3}\sqrt{k_B T/m} \approx 10 \mu m/s$ to swim over its body length l_b.

3.1 Wall approach

Our simulations yield an effect of the wall on the cell swimming velocity in its vicinity. As shown in Fig. 4, we find a slowdown of the velocity normal to the wall already for cell-wall separations larger than a body length.

An important aspect in cell entrapment is the role of hydrodynamic interactions, a fact, which has been addressed in various experiments.[23,44] Experimental studies lead to the conclusion that hydrodynamic interactions are of minor importance.[44] However, other studies show a reduction of the velocity in the direction normal to the surface of an approaching bacteria when closer than approximately a cell length,[22,23,65] which is attributed to an increased friction due to hydrodynamic interactions.[23,66] The far-field approximation for an approaching (externally pulled) sphere yields the normal velocity at a no-slip wall

$$v_y = \bar{v}\left(1 - \frac{9}{16}\frac{d}{y_{cm}} + \frac{1}{16}\left(\frac{d}{y_{cm}}\right)^3\right), \qquad (8)$$

where $\bar{v}$ denotes the velocity far from the boundary (bulk) and y_{cm} the location of the sphere's center.[23,66,67] Our simulation results are in agreement with Eq. (8) within the accuracy of the simulation, cf. Fig. 8.

However, Eq. (8) corresponds to the velocity of an approaching Stokeslet, whereas the near-flow field of an *E. coli* is very different from the Stokeslet flow field.[26] A more suitable approximation would be the normal velocity emerging from the interaction of a

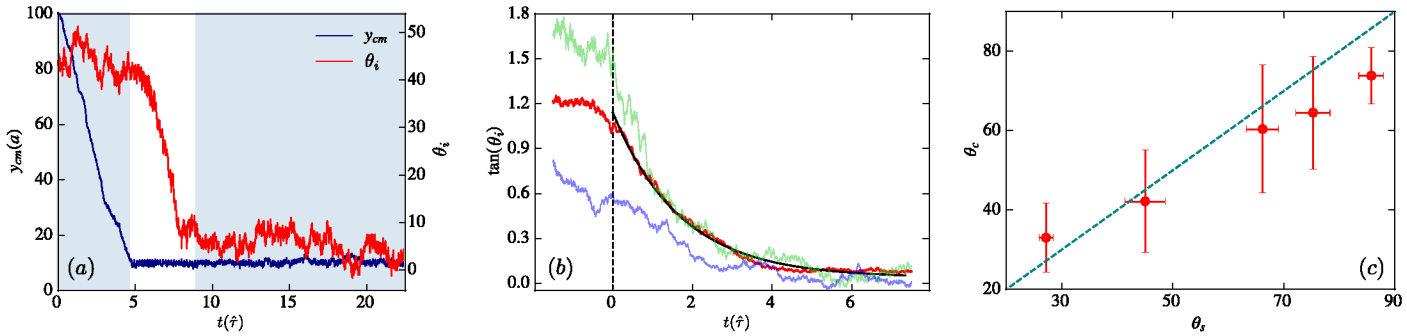

Fig. 3 (a) Time evolution of the center-of-mass position of the cell body above the wall, y_{cm}, and the inclination angle, θ_i, during a wall-entrapment event. (b) Time evolution of the inclination angle during the reorientation stage for a strongly (green) and weakly (blue) wobbling cell for the initial angle 45°. The red curve is the average value over 14 realizations. The dashed line corresponds to the time of collision, t_c, with the wall, and the black solid line is a fit to Eq. (13). (c) Inclination angle at the first encounter with the wall as function of its initial value. The bullets represent average value over all realizations and error bars are the standard deviation. The dashed line indicates $\theta_i = \theta_s$.

hydrodynamic dipole with a no-slip wall, namely

$$v_y^d = -\frac{3p}{64\pi\eta y^2}\left(1-3\sin^2\theta_i\right), \qquad (9)$$

where y is the height of the center of the considered force dipole above the wall, p the dipole strength, where $p>0$ for *E. coli*, η the fluid viscosity, and θ_i the inclination angle.[6,8,68] The actual velocity in then $v_y = \bar{v} + v_y^d$. Normalization with respect to the average swimming velocity $\bar{v}$ and the diameter of the cell body, yields the relation

$$\frac{v_y}{\bar{v}} = 1 - u_0\left(\frac{d}{y}\right)^2. \qquad (10)$$

Using the MPC fluid parameters and the dipole strength $p = 2.2pN\mu m$, obtained in Ref. 26 for swimming *E. coli*, we find $u_0 \approx 2$. As shown in Fig. 4, the velocity contribution of Eq. (10) with $u_0 = 2$ drops somewhat faster for $y_{cm} \to 0$ than the simulation data. However, the data are very well reproduced by fitting Eq. (10), which yields $u_0 = 0.9$. Considering the uncertainties in the determination of the force dipole, specifically in the vicinity of the wall, $u_0 = 2$ is reasonably close to the fitted value, which suggest that the slow-down might be explained by hydrodynamic interactions of the self-propelled cell with the wall. Unfortunately, our data are not precise enough to rule out one of the interactions mechanisms (Eqs. (8), (10)).

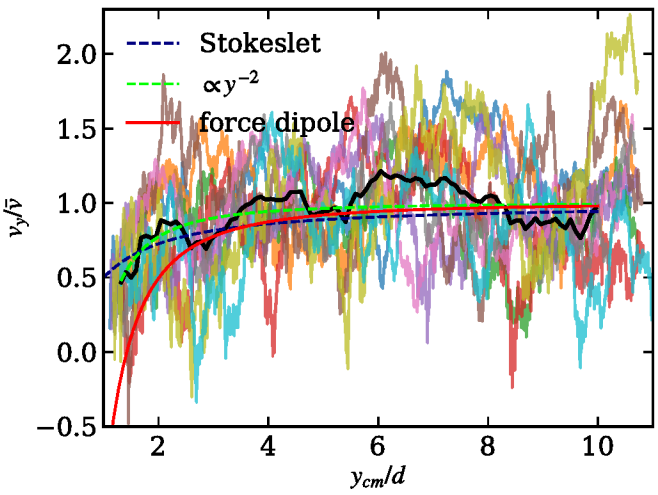

Fig. 4 Velocity normal to the wall as a function of the body center-of-mass position above the wall for various realization and their average (black line); the initial angle is $\theta_s \approx 45°$. The velocities are normalized by the swimming velocity, $\bar{v}$, far from the wall. The purple dashed line is obtained with the Stokeslet velocity of Eq. (8) The red dashed line is calculated with the force-dipole contribution (9), and the green dashed line is a fit of the velocity profile including Eq. (9).

3.2 Impact and scattering

The time dependence of the inclination angle during cell reorientation is displayed in Fig. 3(b) for two realizations of random flagella anchoring, which emphasizes the dependence on the extent of wobbling, as well as the average over several realizations. Two mechanisms contribute to cell reorientation: (i) hydrodynamic interactions with the wall for a force and torque free swimmer and (ii) steric interactions as soon as the swimmer experiences mechanical wall forces.

Hydrodynamic interactions yield the rotation frequency

$$\Omega_z(\theta_i, y) = -\frac{3p\cos\theta_i\sin\theta_i}{64\pi\eta y^3}\left[1+\frac{(\gamma^2-1)}{2(\gamma^2+1)}(1+\sin^2\theta_i)\right], \qquad (11)$$

where γ is the aspect ratio of the cell ($\gamma > 1$).[6,8,68] The influence of the hydrodynamic reorientation on cells can be deduced from Figs. 3, displaying the time dependence of the inclination angle (Fig. 3(b)) and the inclination angle at surface contact, θ_c, as function of the initial angle θ_s (Fig. 3(c)). Figures 3(a), (b) suggest a certain reorientation before a cell encounters the wall, however, by a few degrees only. Similarly, Fig. 3(c) shows small differences between θ_s and θ_c at low θ_s values, but θ_c drops below θ_s at large θ_s as in experiments.[69]

A quantitative comparison of Eq. (11) with the simulation results is hampered by the strong dependence of Ω_z on the height y

above the wall. To account for cell body and flagellar bundle, we use the body length for $y = l_B$, which is approximately equal to the hydrodynamic radius of the cell.[44] With the value $p = 2.2pN\mu m$ for the force dipole and $\gamma = 2.2$ for the aspect ratio of the cell body, Eq. (11) yields $\Omega_z \hat{\tau} \approx -0.8rad \approx -45^\circ$ for $\theta_i = 45^\circ$. This value is approximately 3 times larger than the change in the angle obtained in simulations, 15°, over this time scale, but it is on the right order of magnitude. Hence, hydrodynamic interactions between the swimmer flow field and the wall might play a role in the reorientation dynamics during surface scattering, in contrast to conclusions based on experiments.[23,44].

Steric interactions yield reorientation of the cell after it touched a wall. While interacting with the wall, the cell experiences a repulsive normal force, which is $F_s^\perp = -\gamma_T \bar{v} \sin\theta_i$, i.e., the cell is no longer force free; γ_T is the translational friction coefficient. With the assumption that the propulsion force acts on the center of mass of the cell located at a distance l_{cm} separated from the cell-surface contact point, $F_s^\perp$ implies the torque $M = -\gamma_T \bar{v} l_{cm} \sin\theta_i \cos\theta_i$. Then, the equation of motion $\gamma_R \dot{\theta}_i = M$, γ_R is the rotational friction coefficient, yields

$$\frac{d}{dt} \tan\theta_i = -\gamma_i \tan\theta_i, \tag{12}$$

and, thus, the time dependence

$$\tan\theta_i(t) = \tan\theta_i(0) e^{-\gamma_i t}, \tag{13}$$

where $\gamma_i = \gamma_T \bar{v} l_{cm}/\gamma_R$. Figure 3(b) shows a fit of Eq. (13) to the average of the simulation data. Evidently, the reorientation dynamics is well described by Eq. (13) over the considered time interval for $\gamma_i = 0.6/\hat{\tau} \approx 3/s$. (For the translation of simulation units to physical units, cf. Ref. 26.) Using the above theoretical expression for γ_i, we find $\gamma_i \approx 7.5/s$. Within the uncertainties in the parameters, this value agrees reasonably well with the fit. Moreover, our values are in very good agreement with those obtained in the experiments,[23] where a fit yields $\gamma_i \equiv \kappa' \approx 4.9/s$, and a theoretical estimation $\kappa' \approx 6.3/s$. Thus, the angular momentum, appearing as a consequence of steric interaction as soon as a cell touches a wall, can be responsible for cell reorientation, in agreement with previous studies.[23,44] However, no definite conclusion is possible based in the simulation data, because of the wide uncertainty of parameters entering the rather generic theoretically expressions. For a more precise estimate, a more detailed theoretical approach is needed.

3.3 Surface swimming

During stationary surface migration, the cells progress with their body center-of-mass at nearly constant height. The center-of-mass distribution function, Fig. 5(a), exhibits a peak at a value slightly larger than the body diameter, d, and the width is approximately $d/2$. This large surface separation can only be understood by a significant wobbling dynamics, or a preferred alignment of the body toward or away from the wall, because in a perfectly parallel wall alignment state, the preferred distance should be $y_{cm} \approx d/2$. Moreover, the figure suggest a weak dependence on the starting orientation of the cell. The displayed differences result mainly from lack of sufficient statistics.

Quantitatively, the strong variation of the body orientation is illustrated in Fig. 5(b) for the two snapshots displayed in Figure 6. The latter emphasize the large orientational variations due to the particular (random) arrangement of flagella. In case of the larger variations of θ_b, the distribution function exhibits two peaks indicating a preferred orientation, which in three-dimension corresponds to the swimming direction precessing on a cone. However, this does not affect the overall orientation of the cell, since the average inclination angle is centered around zero with little difference between the two realizations. The distribution function of the inclination angle is presented in Fig. 5(c). Despite the broad distribution of inclination angles with negative values due to wobbling, the overall distribution function depends very little on the initial angle θ_s, as it should be expected, and exhibits a maximum at a positive value. Again, deviations between data for different initial values are of statistical origin. Hence, our simulations reveal a preferred cell orientation toward the wall, in agreement with experimental results[22,23] and simulations,[21] but in contrast to theoretical calculations for a straight, no-wobbling cell,[18,19] which predict an orientation away from the wall.

Interestingly, the large variations in body orientation have little effect on the orientation of the flagella bundle, and hence the overall cell orientation. Evidently, the bundle is quite stable and its rotation dictates the cell-body dynamics rather than vice versa.

To quantify the wobbling motion, we introduce the wobbling angle θ_w as the angle between the major axis of the body and the cell's swimming direction (main axis of the cell's inertia tensor). Figure 7(a) displays the distribution function $P(\theta_w)$ of the wobbling angle for the various realizations. Evidently, we obtain a very broad distribution with the mean value $\theta_w = 46.2^\circ \pm 17.8^\circ$. Experiments yield the smaller average angle $\theta_w \approx 30^\circ$, although the range of angles is comparable.[23] Similarly, simulations of long and highly flagellated cells yield an average value of approximately 30°.[21] Interestingly, we find a roughly bimodal distribution with a peak at about 10° and a very broad peak at about 55°, separated by a pronounced gap at 20°. This could be related to the preferentially organize of the bundle, which is rather well aligned with the cell body, or rather oblique to it. This is in contrast to experimental distributions, which show a high probability for lower angles $< 20^\circ$ and no gap. The discrepancy may be a consequence of the chosen fixed number of flagella, whereas *E. coli* planktonic cells possess approximately $4-7$ flagella. Simulations of swarmer-type cells, with a larger number of flagella, show that the number of flagella matters for bundle formation, and no gap or high probability for small θ_w has been found.[21] Thus, the role of the number of flagella in bundle formation and orientation, from a few to many, needs more detailed investigations.

The scatter plot in Fig. 7(b) collects mean values of the inclination and wobbling angle for the various realizations. For the mean value over all realizations we find $\theta_i = 3.1^\circ \pm 1.4^\circ$. As pointed out before, the positive inclination angle is in agreement with experiments,[22,23] although our value is somewhat smaller. Simulation studies with a single flagellum aligned with the cell body yield the inclination angle $\theta_i \approx 10^\circ$.[70] The larger value could be a consequence of the particular geometry of the applied *E. coli*

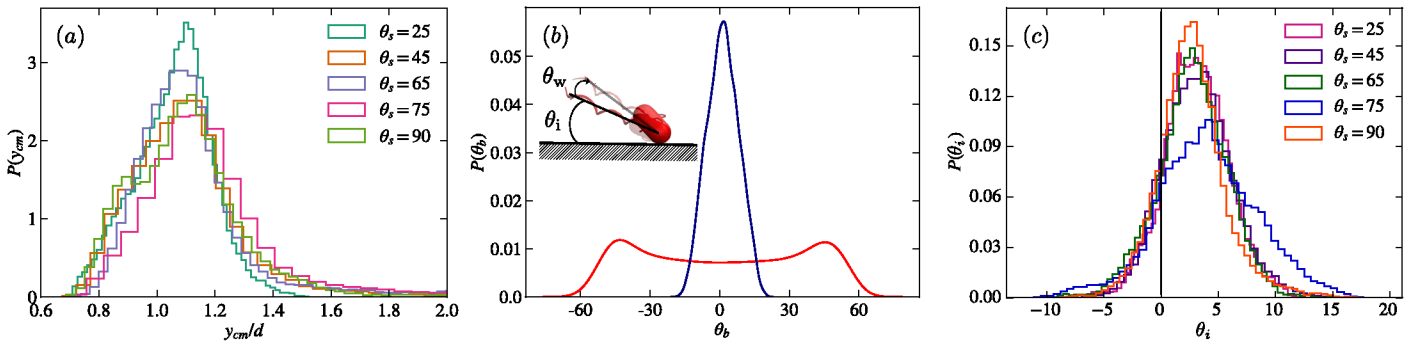

Fig. 5 (a) Distribution function of the body center-of-mass distance from the wall for different initial angles. (b) Distribution of inclination angle for cells with a large (red) and low wobbling (blue) angle. Inset: Definition of inclination and wobbling angle of a cell swimming close to a wall. (c) Distribution function of the inclination angle for cells swimming at surfaces for the indicated starting angles.

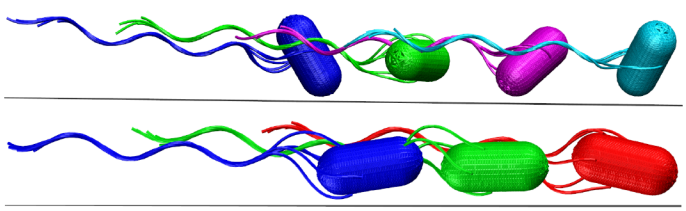

Fig. 6 Snapshots of cells swimming at a wall (black line) for two realizations of flagella arrangements. (Top) The flagella are mainly localized along the equator of the cell body. This leads to a very strong wobbling motion. (Bottom) Example of a cell with flagella preferentially anchored at the rear part of the cell body, which implies weak wobbling. (See supplementary files, movie M2 and M3.)

model, where the helix radius increases toward the rear end of the cell. Since the helix radius is larger than that of the cell, steric flagellum-surface interactions prevent parallel alignment with respect to the surface and imply an orientation toward the wall.

4 Summary and Conclusions

We have analyzed the entrapment dynamics of an *E. coli*-type cell at a no-slip wall by mesoscale hydrodynamic simulations. The random arrangement of (five) flagella on the cell body leads to a strong wobbling motion. The entrapment dynamics can be classified into three phases, a nearly straight approach, reorientation, and surface swimming. We have shown that swimmer-wall hydrodynamic interactions hardly affect the cell orientation as it approaches the wall, since the initial and collisional orientations with respect to the surface change only weakly and can be attributed to fluctuations. The mechanism for the slow-down of the swimming velocity in the vicinity of the wall is less evident due to large scatter in our simulation data. Based on the theoretical models, we can neither rule out the frictional force by an approaching Stokeslet nor the force by the cell's force dipole, because both approaches yield quantitatively reasonable agreement with the simulation results. Similarly, the reorientation of the cell upon touching the wall can be attributed to hydrodynamics and/or a torque emerging from the propulsion force. The extracted hydrodynamic rotation frequency is approximately three times larger than that obtained in simulations. Similarly, rotation by steric interactions is in good quantitative agreement with simulation results. Due to uncertainties in the parameters of the applied theoretical approaches, no definite conclusion about a dominant mechanism is possible based on the simulation data, and both, hydrodynamic and non-hydrodynamic effects, could contribute simultaneously rather than a single mechanism only. A qualitative and quantitative understanding requires a detailed calculation with a more adequate model of a flagellated cell in the vicinity of a wall. Finally, cells swim smoothly along the wall on clockwise circular trajectories, with the major axis of the cell preferentially directed toward the wall. This final state is independent of the initial condition.

The cells exhibit a pronounced wobbling motion, both in bulk and adjacent to a wall. The magnitude of the wobbling angle is determined by the arrangement of the flagella on the cell surface, the further they are away from the poles of the cylindrical body, the stronger the wobbling. In general, the orientation of the flagella bundle dictates the swimming direction, and its rotation determines the alignment of the cell body rather than the other way around. However, the wobbling frequency is equal to the rotation frequency of the body, which is on average $1/5$ of the bundle rotation frequency.

The flagella bundle, which is in our case thinner than the body diameter, is pointing toward the wall, independent of the extent of cell-body angular variations. The cell body orientation is strongly affected by wobbling, but the overall cell orientation is toward the wall. This contradicts theoretical results, which suggest that the inclination of a straight bacterium is pointing away from the wall (negative inclination angle).[18,19] Our simulations suggest that the inclination angle is only weakly affected by the wobbling angle, despite a broad distribution of θ_w, the range of θ_i is rather small. Quantitatively, our simulations yield a somewhat smaller inclination angle than experiments using *E. Coli* bacteria.[22,23] The origin could be specific bacteria-wall interactions not captured in our model, such as particular adhesive sites on the bacteria surface, or interactions with unbundled short flagella.

A characteristics of flagellated bacteria is a large variation of their behavior, depending on various aspects such as number of

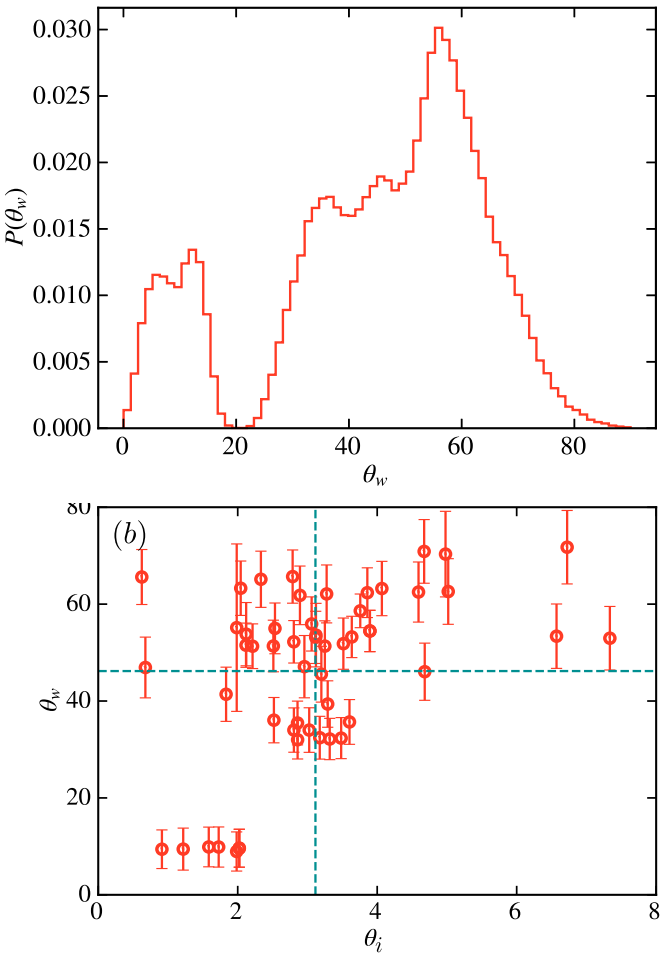

Fig. 7 (a) Distribution function of the wobbling angle θ_w for the applied realizations. (b) Scatter plot of the wobbling and inclination angle θ_i at the wall (different initial angles and their various realizations). The dashed lines indicate the average values.

flagella, flagella arrangement on the cell surface, formation of the bundle, etc.[21] Hence, simulation of a suitable ensemble and extraction of meaning full averages is rather demanding, specifically with a detailed bacterium model as employed in this study. Here, many more in-depth studies are required to achieve a quantitative understanding of swimming bacteria in bulk and at walls.

In summary, our simulations provide insight into the scattering of flagellated bacteria at walls, in particular, into the relevance of swimmer-wall hydrodynamic interactions. We hope that our results, specifically the importance of wobbling, will stimulate comparable experimental studies.

Acknowledgements

Financial support by the Deutsche Forschungsgemeinschaft (DFG) within the priority program SPP 1726 “Microswimmers–from Single Particle Motion to Collective Behaviour” is gratefully acknowledged.

Notes and references

1 J. W. Costerton, Z. Lewandowski, D. E. Caldwell, D. R. Korber and H. M. Lappin-Scott, *Annu. Rev. Microbiol.*, 1995, **49**, 711.
2 E. Lauga, *Annu. Rev. Fluid Mech.*, 2016, **48**, 105.
3 R. Hartmann, P. K. Singh, P. Pearce, R. Mok, B. Song, F. Díaz-Pascual, J. Dunkel and K. Drescher, *Nat. Phys.*, 2019, **15**, 251.
4 H.-C. Flemming, J. Wingender, U. Szewzyk, P. Steinberg, S. A. Rice and S. Kjelleberg, *Nat. Rev. Microbiol.*, 2016, **14**, 563 EP.
5 H. Koo, R. N. Allan, R. P. Howlin, P. Stoodley and L. Hall-Stoodley, *Nat. Rev. Microbiol.*, 2017, **15**, 740 EP.
6 A. P. Berke, L. Turner, H. C. Berg and E. Lauga, *Phys. Rev. Lett.*, 2008, **101**, 038102.
7 Rothschild, *Nature*, 1963, **198**, 1221.
8 S. E. Spagnolie and E. Lauga, *J. Fluid Mech.*, 2012, **700**, 105–147.
9 J. Elgeti and G. Gompper, *Eur. Phys. J. Spec. Top.*, 2016, **225**, 2333.
10 J. Elgeti, R. G. Winkler and G. Gompper, *Rep. Prog. Phys.*, 2015, **78**, 056601.
11 O. Sipos, K. Nagy, R. Di Leonardo and P. Galajda, *Phys. Rev. Lett.*, 2015, **114**, 258104.
12 J. Happel and H. Brenner, *Low Reynolds number hydrodynamics: with special applications to particulate media*, Springer Science & Business Media, 1983.
13 D. Das and E. Lauga, *Phys. Rev. E*, 2019, **100**, 043117.
14 E. Lauga, W. R. DiLuzio, G. M. Whitesides and H. A. Stone, *Biophys. J.*, 2006, **90**, 400 – 412.
15 G. Li and J. X. Tang, *Phys. Rev. Lett.*, 2009, **103**, 078101.
16 G. Li, J. Bensson, L. Nisimova, D. Munger, P. Mahautmr, J. X. Tang, M. R. Maxey and Y. V. Brun, *Phys. Rev. E*, 2011, **84**, 041932.
17 J. Elgeti and G. Gompper, *EPL*, 2009, **85**, 38002.
18 H. Shum, E. A. Gaffney and D. J. Smith, *Proc. R. Soc. A*, 2010, **466**, 1725–1748.
19 D. Pimponi, M. Chinappi, P. Gualtieri and C. M. Casciola, *J. Fluid Mech.*, 2016, **789**, 514–533.
20 J. Hu, A. Wysocki, R. G. Winkler and G. Gompper, *Sci. Rep.*, 2015, **5**, 9586.
21 T. Eisenstecken, J. Hu and R. G. Winkler, *Soft Matter*, 2016, **12**, 8316.
22 S. Bianchi, F. Saglimbeni and R. Di Leonardo, *Phys. Rev. X*, 2017, **7**, 011010.
23 S. Bianchi, F. Saglimbeni, G. Frangipane, D. Dell’Arciprete and R. Di Leonardo, *Soft Matter*, 2019, **15**, 3397.
24 S. Palagi and P. Fischer, *Nat. Rev. Mater.*, 2018, **3**, 113.
25 G. Gompper, R. G. Winkler, T. Speck, A. Solon, C. Nardini, F. Peruani, H. Löwen, R. Golestanian, U. B. Kaupp, L. Alvarez, T. Kiørboe, E. Lauga, W. C. K. Poon, A. DeSimone, S. Muiños-Landin, A. Fischer, N. A. Söker, F. Cichos, R. Kapral, P. Gaspard, M. Ripoll, F. Sagues, A. Doostmohammadi, J. M. Yeomans, I. S. Aranson, C. Bechinger, H. Stark, C. K. Hemelrijk, F. J. Nedelec, T. Sarkar, T. Aryaksama, M. Lacroix, G. Duclos, V. Yashunsky, P. Silberzan, M. Arroyo and S. Kale, *J. Phys: Condens. Matter*, 2020, **32**, 193001.
26 J. Hu, M. Yang, G. Gompper and R. G. Winkler, *Soft Matter*, 2015, **11**, 7867.
27 M. Ripoll, K. Mussawisade, R. G. Winkler and G. Gompper,

Europhys. Lett., 2004, **68**, 106.
28 A. Malevanets and R. Kapral, *J. Chem. Phys.*, 1999, **110**, 8605.
29 R. Kapral, *Adv. Chem. Phys.*, 2008, **140**, 89.
30 G. Gompper, T. Ihle, D. M. Kroll and R. G. Winkler, *Adv. Polym. Sci.*, 2009, **221**, 1.
31 I. O. Götze and G. Gompper, *Phys. Rev. E*, 2010, **82**, 041921.
32 D. J. Earl, C. M. Pooley, J. F. Ryder, I. Bredberg and J. M. Yeomans, *J. Chem. Phys.*, 2007, **126**, 064703.
33 J. Elgeti, U. B. Kaupp and G. Gompper, *Biophys. J.*, 2010, **99**, 1018.
34 S. B. Babu and H. Stark, *New J. Phys.*, 2012, **14**, 085012.
35 J. Elgeti and G. Gompper, *Proc. Natl. Acad. Sci. USA*, 2013, **110**, 4470.
36 M. Theers and R. G. Winkler, *Phys. Rev. E*, 2013, **88**, 023012.
37 M. Yang and M. Ripoll, *Soft Matter*, 2014, **10**, 1006.
38 A. Zöttl and H. Stark, *Phys. Rev. Lett.*, 2014, **112**, 118101.
39 K. Qi, E. Westphal, G. Gompper and R. G. Winkler, *Phys. Rev. Lett.*, 2020, **124**, 068001.
40 Y. Yang, J. Elgeti and G. Gompper, *Phys. Rev. E*, 2008, **78**, 061903.
41 S. Y. Reigh, R. G. Winkler and G. Gompper, *Soft Matter*, 2012, **8**, 4363.
42 S. Y. Reigh, R. G. Winkler and G. Gompper, *PLoS ONE*, 2013, **8**, e70868.
43 M. Theers, E. Westphal, K. Qi, R. G. Winkler and G. Gompper, *Soft Matter*, 2018, **14**, 8590.
44 K. Drescher, J. Dunkel, L. H. Cisneros, S. Ganguly and R. E. Goldstein, *Proc. Natl. Acad. Sci. USA*, 2011, **108**, 10940.
45 Y. Hyon, u. Marcos, T. R. Powers, R. Stocker and H. C. Fu, *J. Fluid Mech.*, 2012, **705**, 58–76.
46 *Helical Wormlike Chains in Polymer Solutions*, ed. H. Yamakawa and T. Yoshizaki, Springer Verlag, Berlin Heidelberg, 1997.
47 R. Vogel and H. Stark, *Eur. Phys. J. E*, 2010, **33**, 259–271.
48 N. C. Darnton, L. Turner, S. Rojevsky and H. C. Berg, *J. Bacteriol.*, 2007, **189**, 1756–1764.
49 M. P. Allen and D. J. Tildesley, *Computer Simulation of Liquids*, Clarendon Press, Oxford, 1987.
50 M. Theers, E. Westphal, G. Gompper and R. G. Winkler, *Phys. Rev. E*, 2016, **93**, 032604.
51 H. Noguchi and G. Gompper, *Phys. Rev. E*, 2008, **78**, 016706.
52 M. Theers and R. G. Winkler, *Soft Matter*, 2014, **10**, 5894.
53 T. Ihle and D. M. Kroll, *Phys. Rev. E*, 2003, **67**, 066705.
54 C.-C. Huang, A. Varghese, G. Gompper and R. G. Winkler, *Phys. Rev. E*, 2015, **91**, 013310.
55 K. Mussawisade, M. Ripoll, R. G. Winkler and G. Gompper, *J. Chem. Phys.*, 2005, **123**, 144905.
56 S. Poblete, A. Wysocki, G. Gompper and R. G. Winkler, *Phys. Rev. E*, 2014, **90**, 033314.
57 A. Lamura, G. Gompper, T. Ihle and D. M. Kroll, *Europhys. Lett.*, 2001, **56**, 319–325.
58 R. M. Berry and H. C. Berg, *Proc. Natl. Acad. Sci. USA*, 1997, **94**, 14433–14437.
59 D. Das and E. Lauga, *Soft Matter*, 2018, **14**, 5955.
60 B. Liu, M. Gulino, M. Morse, J. X. Tang, T. R. Powers and K. S. Breuer, *Proc. Natl. Acad. Sci. USA*, 2014, **111**, 11252.
61 N. C. Darnton, L. Turner, S. Rojevsky and H. C. Berg, *J. Bacteriol.*, 2007, **189**, 1756–1764.
62 L. Turner, R. Zhang, N. C. Darnton and H. C. Berg, *J. Bacteriol.*, 2010, **192**, 3259.
63 A. E. Patteson, A. Gopinath, M. Goulian and P. E. Arratia, *Sci. Rep.*, 2015, **5**, 15761.
64 Y. Hyon, Marcos, T. R. Powers, R. Stocker and H. C. Fu, *J. Fluid Mech.*, 2012, **705**, 58–76.
65 P. D. Frymier, R. M. Ford, H. C. Berg and P. T. Cummings, *Proc. Natl. Acad. Sci. USA*, 1995, **92**, 6195.
66 M. Ramia, D. L. Tullock and N. Phan-Thien, *Biophys. J.*, 1993, **65**, 755.
67 S. Kim and S. J. Karrila, *Microhydrodynamics: principles and selected applications*, Butterworth-Heinemann, Boston, 1991.
68 R. G. Winkler and G. Gompper, *Handbook of Materials Modeling: Methods: Theory and Modeling. Springer*, 2018, 1–20.
69 S. Bianchi, F. Saglimbeni and R. Di Leonardo, *Phys. Rev. X*, 2017, **7**, 011010.
70 A. J. T. M. Mathijssen, N. Figueroa-Morales, G. Junot, E. Clement, A. Lindner and A. Zöttl, *Nat. Commun.*, 2019, **20**, 3434.